International Journal of Innovative Research and Scientific Studies, 8(11) 2025, pages: 501-512

IJIRSS
International Journal of Innovative Research & Scientific Studies

ISSN: 2617-6548

URL: www.ijirss.com

Study of gas and shrinkage porosity in Al-Si die cast couplings using X-ray micro-computed tomography

Felipe Díaz[1*], Boris Riva[2], Matías Peralta[3]

[1]*Departamento de Ingeniería Electromecánica, Universidad Tecnológica Nacional-Facultad Regional Rafaela-CONICET, Acuña 49, Rafaela, Santa Fe, Argentina.*
[2]*Departamento de Ingeniería Industrial, Universidad Tecnológica Nacional-Facultad Regional Rafaela, Acuña 49, Rafaela, Santa Fe, Argentina.*
[3]*Departamento de Validación de Equipos y Componentes, Instituto Nacional de Tecnología Industrial-Centro Litoral, Ruta Nacional N°34 km 227,6, Rafaela, Santa Fe, Argentina.*

Corresponding author: Felipe Díaz (*Email: felipe.diaz@frra.utn.edu.ar*)

Abstract

The purpose of this work is to demonstrate the feasibility of a quantitative methodology to study 3D porosity in two Al-Si die cast couplings from an air-suspension system of heavy-duty vehicles, using X-ray micro-computed tomography and digital image processing. Although both parts are homologous, one was rejected for commercialisation due to a leak detected during a pneumatic test. The image post-processing, carried out using VGSTUDIO MAX 3.0 software, enabled the design of a strategy to evaluate and compare pore subpopulations in regions of interest (ROIs) of both parts. Based on the compactness parameter, it was possible to segment pore subpopulations according to their origin: gas and shrinkage. The results shows that the gas porosity volumes in the ROIs of both parts are similar. However, the shrinkage porosity volume is higher in the ROI of the rejected part, which involves changes introduced in the mould filling pressure and/or speed that affected solidification in this part. Finally, the quantitative methodology proposed in this work could be a valuable tool in the stages of research, product development, and quality control of both cast parts and other porous components obtained from different manufacturing processes.

Keywords: Al-Si alloy, Die-casting, Non-destructive evaluation, Porosity, X-ray tomography.

DOI: 10.53894/ijirss.v8i11.10962
Funding: This research has been supported by grants awarded by UTN-SICyT (PID MAECARA0008439.
History: Received: 8 October 2025 / **Revised:** 13 November 2025 / **Accepted:** 18 November 2025 / **Published:** 27 November 2025

Competing Interests: The authors declare that they have no competing interests.
Authors' Contributions: All authors contributed equally to the conception and design of the study. All authors have read and agreed to the published version of the manuscript.
Transparency: The authors confirm that the manuscript is an honest, accurate, and transparent account of the study; that no vital features of the study have been omitted; and that any discrepancies from the study as planned have been explained. This study followed all ethical practices during writing.
Acknowledgments: The authors wish to express their sincere gratitude to Diego Pollini for his great willingness and help regarding the couplings evaluated in this work.
Publisher: Innovative Research Publishing

1. Introduction

Al-Si die-casting is a production process by which this alloy is injected at high pressure into a mould to obtain parts of complex design and geometry. Silicon is a key element in this alloy, as it reduces the melting point, increases fluidity, and improves resistance to high temperatures [1]. This casting process, efficient for mass production, offers several advantages: good dimensional accuracy, good surface finish, and little need for further machining. Numerous automotive, aerospace and communications components, requiring high strength-to-weight ratio, good corrosion resistance and/or high thermal conductivity, are manufactured via Al-Si die-casting [2-4]. However, the greater or lesser porosity associated with this process is always a concern because it could alter different mechanical properties [5]. Even so, for components where tightness is the most important requirement, porosity could be more tolerated.

If the porosity associated with the die-casting process exceeds a permissible volumetric value, it could cause failures in parts that, in service, interact with fluids subjected to medium or high pressure. Defects producing fluid leaks could have their origin in: excess air during mould filling, the release of gases and/or defects in the mould feeding. These defects would produce shrinkage porosity that could open leak paths in zones of the solidified part, which do not present regularity in their shape or specific zones of occurrence [6]. The micro-mechanisms of formation of these defects have been analysed in the literature [7-11]. It is worth noting that the presence of shrinkage porosity, unlike that generated by gases, is always accompanied by porosity in adjacent areas. In the interdendritic regions, which take longer to solidify, sufficient spaces would be generated that could constitute potential escape channels for fluids [1].

On the other hand, traditional non-destructive evaluation techniques, including radiography and ultrasound, provide good porosity visualisation, characterisation, and diagnosis capabilities. However, at the stages of research, product development, prototyping, and also in the inspection and quality control of castings, more efficient techniques are required to assess the nature, extent, and distribution of porosity. An advanced non-invasive technique for evaluation of defects, porosity, and structural integrity of cast components is X-ray micro-computed tomography (µCT) [12-14]. This technique generates multiple data sets from the attenuation of X-rays as they pass through the solid being evaluated at different rotational positions. A complex algorithm then processes the generated data at each angular position to reconstruct the 3D volume of the solid [15, 16]. It is worth noting that digital image processing techniques associated with µCT allow performing multiple quantitative assessments to characterise, individually and collectively, a large number of pores, both quasi-spherical and irregular in shape, according to their spatial coordinates, surface area, volume, shape, and nearest neighbour distances. Regarding shape, these digital processing techniques allow evaluating each pore using the compactness parameter (C), which is obtained from the pore volume (V) and the volume of the sphere surrounding the pore (Vs)

$$C = V/Vs \quad (1)$$

It is worth noting that this shape parameter was exhaustively evaluated and identified as a very accurate geometric parameter, even superior to the sphericity parameter [17, 18].

This paper presents, compares, and discusses the results of 3D porosity characterisation and visualization, obtained via µCT and digital image processing, in homologous parts of Al-Si die-casting corresponding to an air-suspension system of heavy-duty vehicles. Although porosity does not affect the mechanical strength of these parts, and the pore count is similar in both, only one part was considered acceptable according to the production parameters of structural integrity. The other part was rejected for commercialisation because it did not meet the tightness requirements. The quantitative methodology proposed in this work includes 3D reconstruction of the evaluated solid, visualisation of defects in different planes and regions of interest, 3D defect evaluation via transparencies, and a comprehensive study of the compactness parameter distributions. The use of this geometric parameter enabled the exhaustive analysis of pore subpopulations segmented by their origin (gas and shrinkage) and size, a phenomenon not yet examined in the literature via this accurate parameter. Finally, the methodology proposed in this work allowed correlating the results obtained via µCT with the production process from which the parts were obtained.

2. Materials and Methods

2.1. Die Cast Components

In this work, two homologous Al-Si die cast couplings are evaluated. The coupling is located between the compressed air supply system and the air-ride suspension system of heavy vehicles [19]. The dimensions are 68 x 35 x 35 mm. One of the couplings is classified as apt (A) and the other as not apt (NA) for commercialisation. Figure 1 shows a 3D image of the A part, which has inlet and outlet zones for compressed air, as well as a vent cone. In these lines, tightness is essential for maintaining air pressure in service. It is worth noting that the vent cone acts as a safety valve incorporating a diaphragm. When the air-ride suspension system is subjected to backpressure due to uneven ground, the diaphragm will activate, releasing excess air pressure [20].

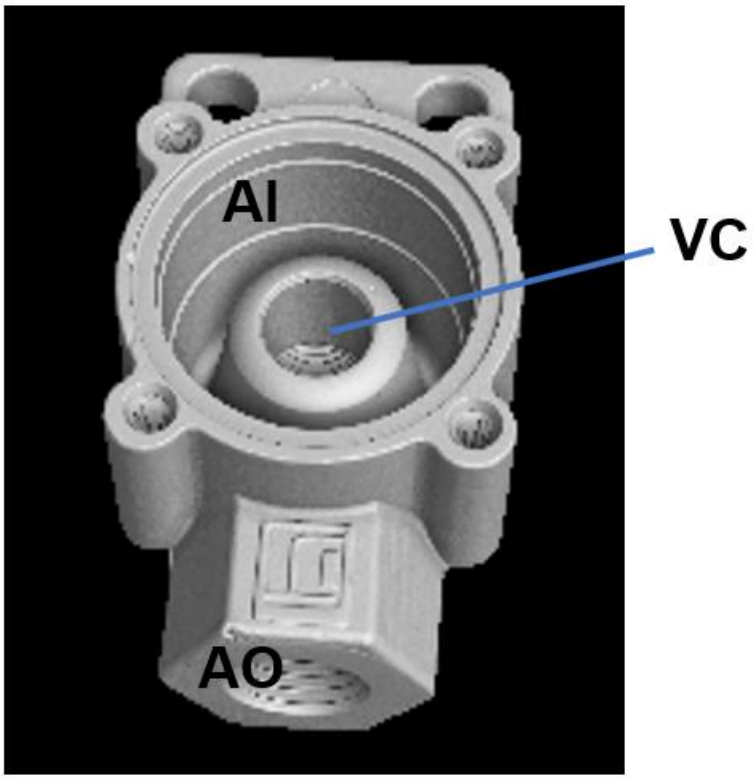

Figure 1.
Accepted part (AI, air inlet; AO, air outlet; VC, vent cone).

The die-casting process for manufacturing these components, carried out at an auto parts company (Rafaela, Argentina), can be divided into phases. Figure 2 shows a production process diagram. First, the Al-Si alloy used as raw material (ALCOA 380) is heated in a furnace to 680°C and poured into a pan, from which the amount of molten material needed for each injection is taken. The chemical composition of the Al-Si alloy is shown in Table 1. Then, the action of a piston injects the material into the mould. It is worth noting that each parameter, such as injection pressure, will directly influence the pore network generated. The part is then released and subjected to different processes to determine whether it is accepted for commercialization. First, shot peening is performed to clean the outer surface. Then, the threaded holes required for service and to carry out the next process are machined. This process involves impregnating the coupling with a sodium silicate compound to seal potential leaks. In the final phase, a pneumatic test was performed to evaluate the tightness of the lines. This test involves injecting compressed air at 5 bar through the inlet opening (see Figure 1), hermetically sealing the outlet and verifying the pressure drop after 30 seconds. If the drop is greater than 0.03 bar, the coupling is rejected and will not be commercialised.

2.2. X-Ray Micro-Tomography

To select the optimal parameters for the micro-tomography process, the density, geometry, and dimensions of the components to be scanned were evaluated. In addition, the general characteristics and state of the scanner and the level of wear of its consumables parts were also taken into account. The couplings were scanned using a General Electric scanner (Phoenix V |tome| x S 240), with an acceleration voltage of 170 kV and a filament current of 100 µA. The magnification and resolution parameters were 2.04x and 97 µm/voxel, respectively. Scanning each coupling took approximately 1 hour and consisted of recording 1000 projections, with three frames averaged for each projection. Using a ball bar type distance pattern, a dimensional adjustment of the scanner was carried out before scanning the couplings [21].

It is worth noting that, in the process of acquiring a tomographic image, the preferential absorption of low-energy X-rays generates beam hardening [22, 23] which can produce different distortions in the 3D image called artefacts [24, 25]. Because the scanned parts are small and made of Al-Si alloy, which has low density, it was not necessary to carry out a physical or hardware filtering for the removal of low-energy X-rays. However, from the 3D image reconstruction software, a digital removal of the generated artefacts was carried out by applying a beam hardening correction filter. This filter causes the brightness values in each voxel of the 3D reconstruction to tend to be similar.

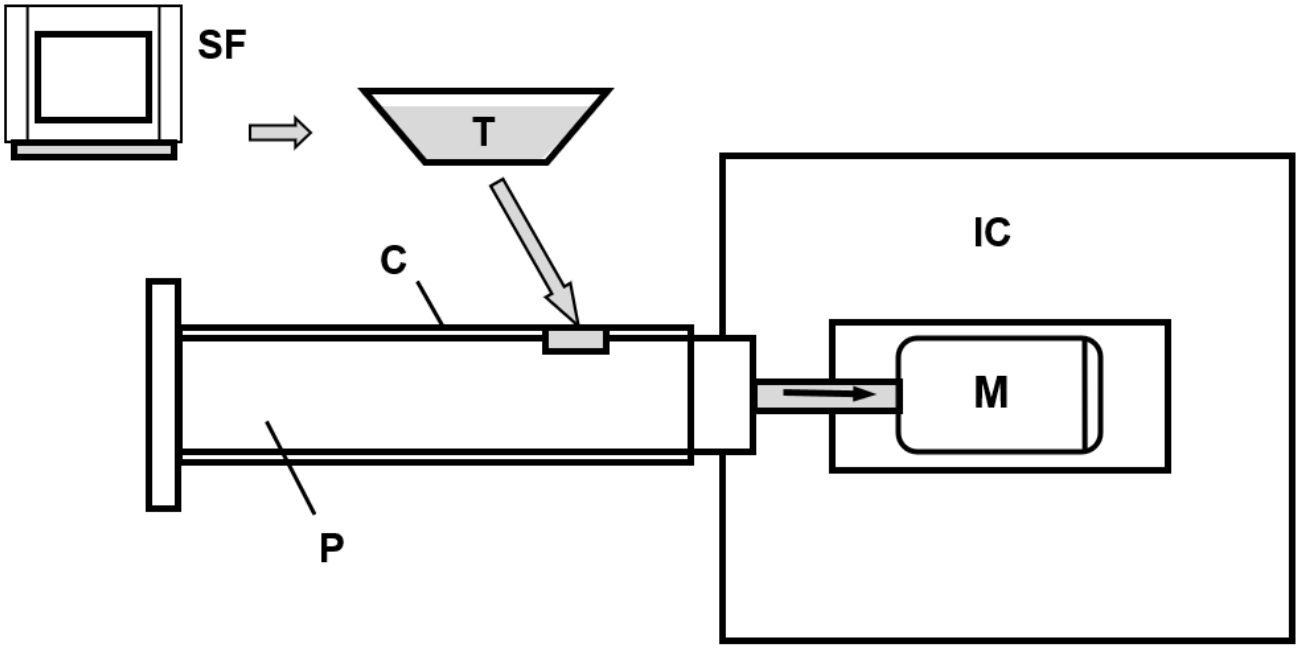

Figure 2.
Casting process diagram (SF: smelting furnace, T: tray, C: cylinder, M: mould, P: piston, IC: injection chamber).

Table 1.
Chemical composition of ALCOA 380.

Chemical composition (wt %)						
Si	**Cu**	**Zn**	**Fe**	**Mn**	**Mg**	**Al**
9	3.5	1.3	0.85	0.5	0.4	balance

2.3. Pore Characterization

In the couplings, the pores were characterised by their shape, size, relative position, and distribution. The vent cone (see Figure 1) was evaluated as a region of interest (ROI) because the probability of leak paths is higher in this region. Several pore subpopulations corresponding to this ROI were also studied to correlate the detected porosity with the die-casting process. The morphological, volumetric, and distributional analysis of the pores in both couplings was performed using Volume Graphics VGSTUDIO MAX 3.0 (version 3.0, Volume Graphics, Heidelberg, Germany) [26] a software commonly used in µCT laboratories. The different pore subpopulations were segmented using the VGDefX™ algorithm, a VGSTUDIO MAX 3.0 subroutine.

On the other hand, volume and compactness distributions were evaluated in different pore subpopulations using VGDefX™. As mentioned above, compactness is an important parameter that allows evaluating the geometry of each pore. According to Equation 1, the C value for a spherical pore is equal to 1. Since a pore in a real material is never a sphere, C values will always be less than 1. Figure 3 shows pore morphologies of both couplings retrieved from the VGDefX™ algorithm. This figure shows that C values increase as the pore shape tends to be a sphere.

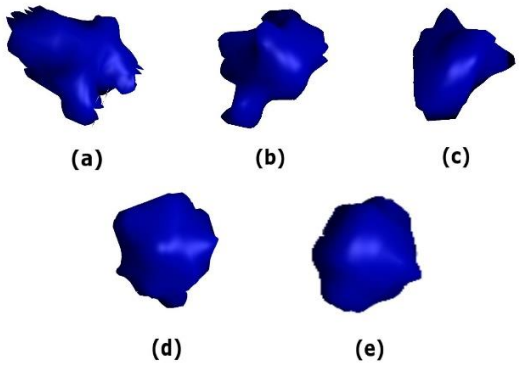

Figure 3.
Random pores from both ROIs. The values of the compactness parameter are: (a) C = 0.25, (b) C = 0.35, (c) C = 0.45, (d) C = 0.55 and (e) C = 0.65.

2.4. Gap Definition

The Gap parameter was also evaluated in this work. This parameter measures the distance between a pore and its nearest neighbour. As shown in Figure 4, the measurement is performed from the surfaces of the circumscribed spheres of both pores. For the ideal case of spherical pores, the Gap will always be positive, or zero if both spheres intersect at a point.

However, because real pores are never spherical, the Gap value will be negative when the circumscribed spheres intersect. If the Gap value is positive, it will increase as the neighbouring pores are distanced. Conversely, if it is negative, it will increase as the irregularity of nearby pores increases. Therefore, the Gap provides information about the greater or lesser tendency of pores to generate clusters and also about the shape irregularity of neighbouring pores.

3. Results and Discussion

3.1. Vent Cone Porosity

Figure 5a shows an image corresponding to a longitudinal plane of the A part. It is worth noting that this part contains four holes and the threading of the air outlet duct, which were manufactured after the part was accepted for commercialisation. The image clearly shows that the most affected region is in the walls of the vent cone. Figure 5b shows an image generated from a vertical section plane of the A part. This plane also shows the affected vent cone, which will be evaluated in this work as a ROI using VGSTUDIO MAX 3.0 software.

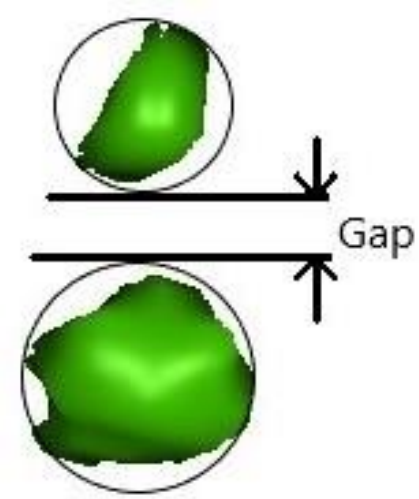

Figure 4.
Schematic representation of the Gap parameter.

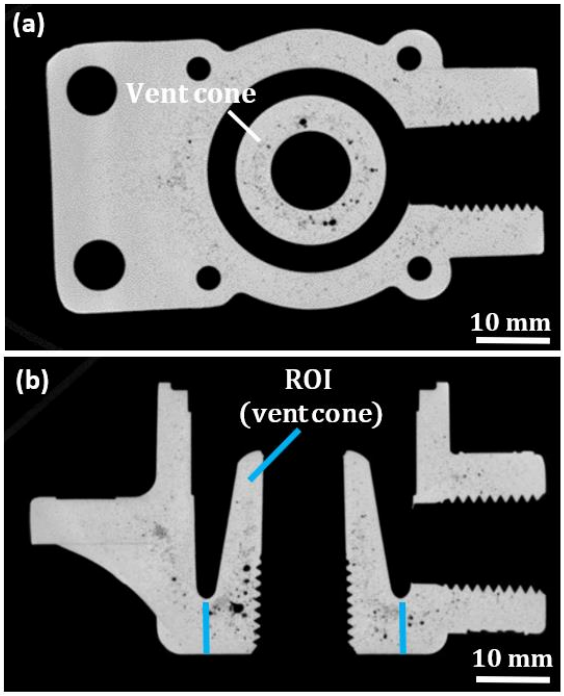

Figure 5.
(a) Horizontal and (b) vertical slices of the accepted part.

3.2. 3D evaluation of ROIs

The compactness value of 0.5 can be established as the limit between quasi-spherical and irregular shapes [17, 18]. Figure 3, which shows different pore morphologies and their values of compactness, corroborates this limit value. In this work, quasi-spherical pores, originating from gases retained in the alloy in its liquid state [7] will be associated with

compactness values greater than 0.5. On the other hand, irregular pores, generated by shrinkage due to poor solidification [6] will have compactness values less than 0.5.

Figure 6 shows gas (C>0.5) and shrinkage (C<0.5) porosity for the ROIs of both parts. Figures 6a and 6c, corresponding to gas porosity, show small pores and corroborate the quasi-spherical shape of them. In both ROIs, the porosity is uniformly distributed with some zones of concentration. It is worth noting that, in the A part, solidification was most efficient at the end of the liquid metal feed path (upper zone of the cone). Figure 6b shows shrinkage pores in the ROI of the A part. These pores are irregularly shaped, widely spaced, and further away from the top edge and the outer surface. In contrast, the pores in the other ROI (Figure 6d) form blocks or clusters near the inner edge. From these clusters, a high count can be predicted for small Gap values, both positive and negative. The pores in this ROI are distanced from the outer surface, starting at the bottom edge. It is worth noting that the pore count is low at the top edge of the cone.

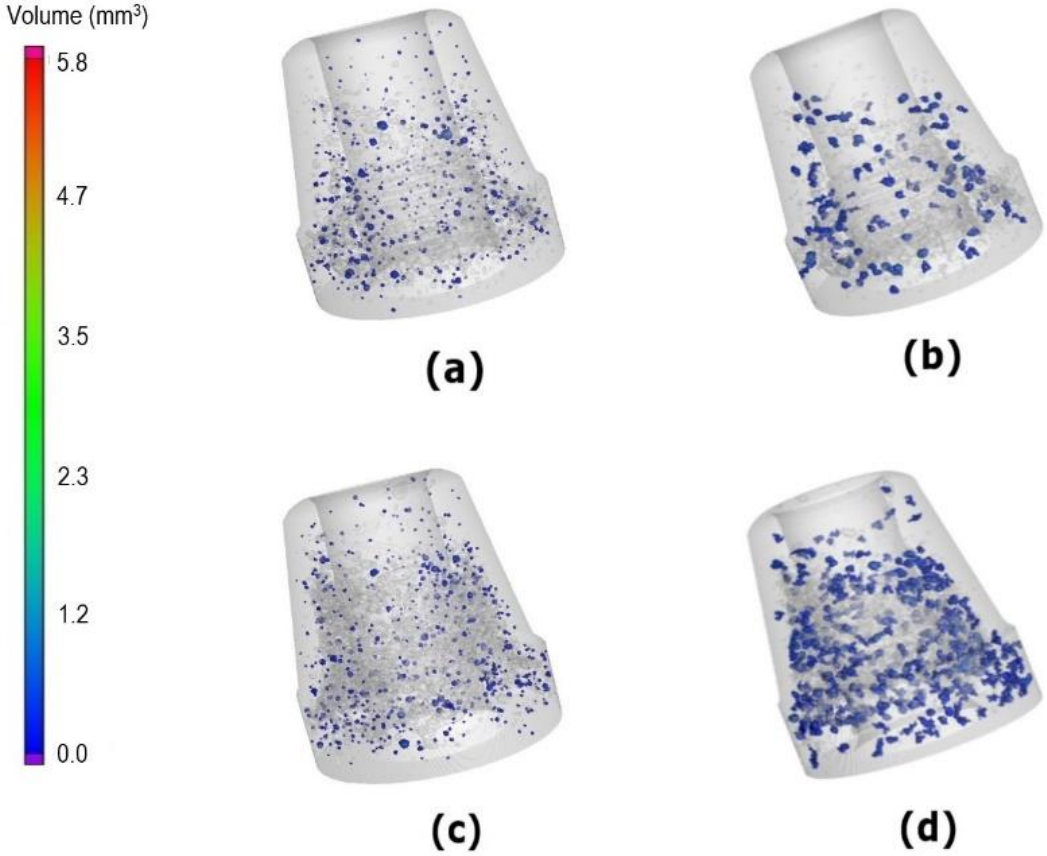

Figure 6.
(a) Gas and (b) shrinkage porosity in the A part ROI. (c) Gas and (d) shrinkage porosity in the NA part ROI. The shrinkage porosity is evaluated in the 0.2-0.6 mm^3 volume range.

3.3. Pore Distribution Evaluation

Because more than 99% of the pores in both ROIs have a volume corresponding to the 0-0.6 mm^3 range, different pore populations and subpopulations corresponding to this value range were analysed. Figure 7 shows the volume distributions for the ROIs of both parts. In both cases, the distribution is hyperbolic, with high pore count in the 0-0.1 mm^3 range (small pores). It is possible to notice that the pore population corresponding to the NA part has a higher pore count in the 0-0.3 mm^3 range. Figure 8 shows the compactness as a function of pore volume. In these graphs, each pore is represented by a blue circle. Different concentration zones can be observed in these graphs. In the A part (Figure 8a), this zone is quasi-triangular and corresponds to the 0-0.2 mm^3 range. In the NA part (Figure 8b), the concentration zone extends the range to 0-0.3 mm^3. Furthermore, the extension of the concentration zone includes low compactness pores (0.05-0.3 compactness range). Therefore, these pores are generated by shrinkage [6].

3.4. Subpopulation Analysis

Figure 9a shows the pore counts for gas-generated (C>0.5) and shrinkage-generated (C<0.5) subpopulations for both ROIs. As expected, the shrinkage pore count is high compared to the gas-generated pore count. The ROI of the A part has a higher number of shrinkage pores. In contrast, the ROI of the NA part has a higher gas pore count. Figure 9b shows the volume occupied by porosity in both ROIs for the same subpopulations. Considering only gas-generated pores, the volume is similar for both ROIs. Therefore, the gas-generated pores, whose volume is low, will not generate leak-tightness problems. In contrast, for shrinkage pores, the porosity volume of the NA part ROI is significantly larger than that of the A

part ROI, despite the latter having more pores. As expected, fluid leakage problems would be linked to the fact that the shrinkage porosity volume in a critical zone (ROI) would exceed the permissible limit.

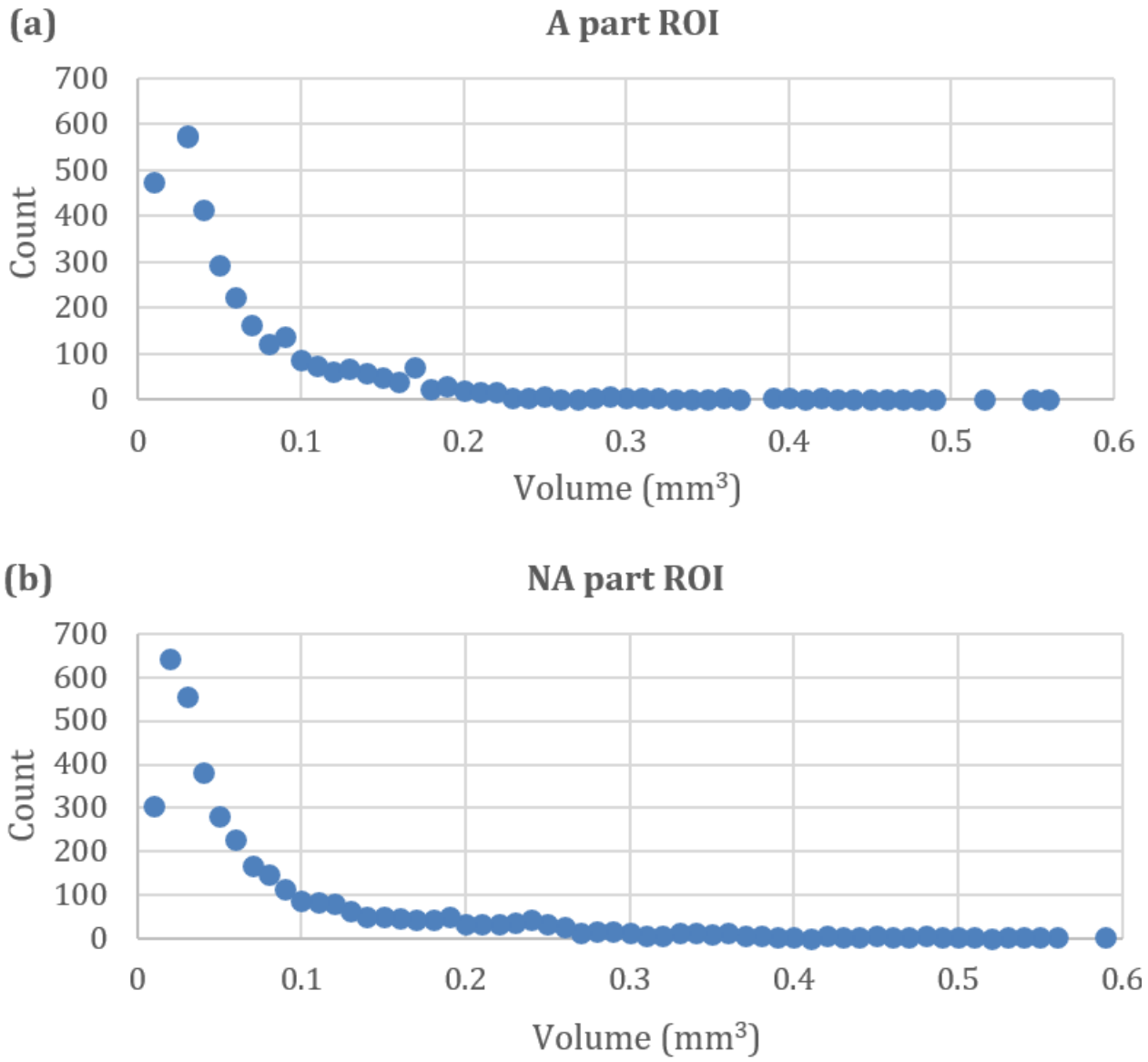

Figure 7.
Volume distributions of the (a) A and (b) NA part ROIs.

Table 2 contains porosity count and volume values. The pore count is similar for both ROIs. The percentage values for gas and shrinkage pore counts are also similar. In contrast, the difference in porosity volume between the ROIs is significant (105.8 mm³). However, the percentage values for gas and shrinkage pore volume are similar in both ROIs. Taking into account the shrinkage pores, the volume difference between the two ROIs is 104.9 mm³. This value would explain the pressurised air leaks that only occur in the NA part. On the other hand, the average value of the volume corresponding to shrinkage pores is 0.073 mm³ for the A part and 0.114 mm³ for the NA part, the latter value being 56% higher.

3.5. Small, Medium and Large Pore Analysis

In this work, pore subpopulations generated according to a size criterion were also analysed. Small, medium, and large pores, corresponding to the following volume ranges: 0–0.1 mm³, 0.1–0.2 mm³, and 0.2–0.6 mm³, respectively, were evaluated. Figure 10a shows a high count of small shrinkage pores, with the highest corresponding to the A part ROI. Regarding medium and large pores, as might have been predicted, the highest count corresponds to the NA part. On the other hand, the count of small pores, generated by gases (Figure 10b), is very high for both subpopulations, and, in addition, the count for the medium and large pore subpopulations is very low.

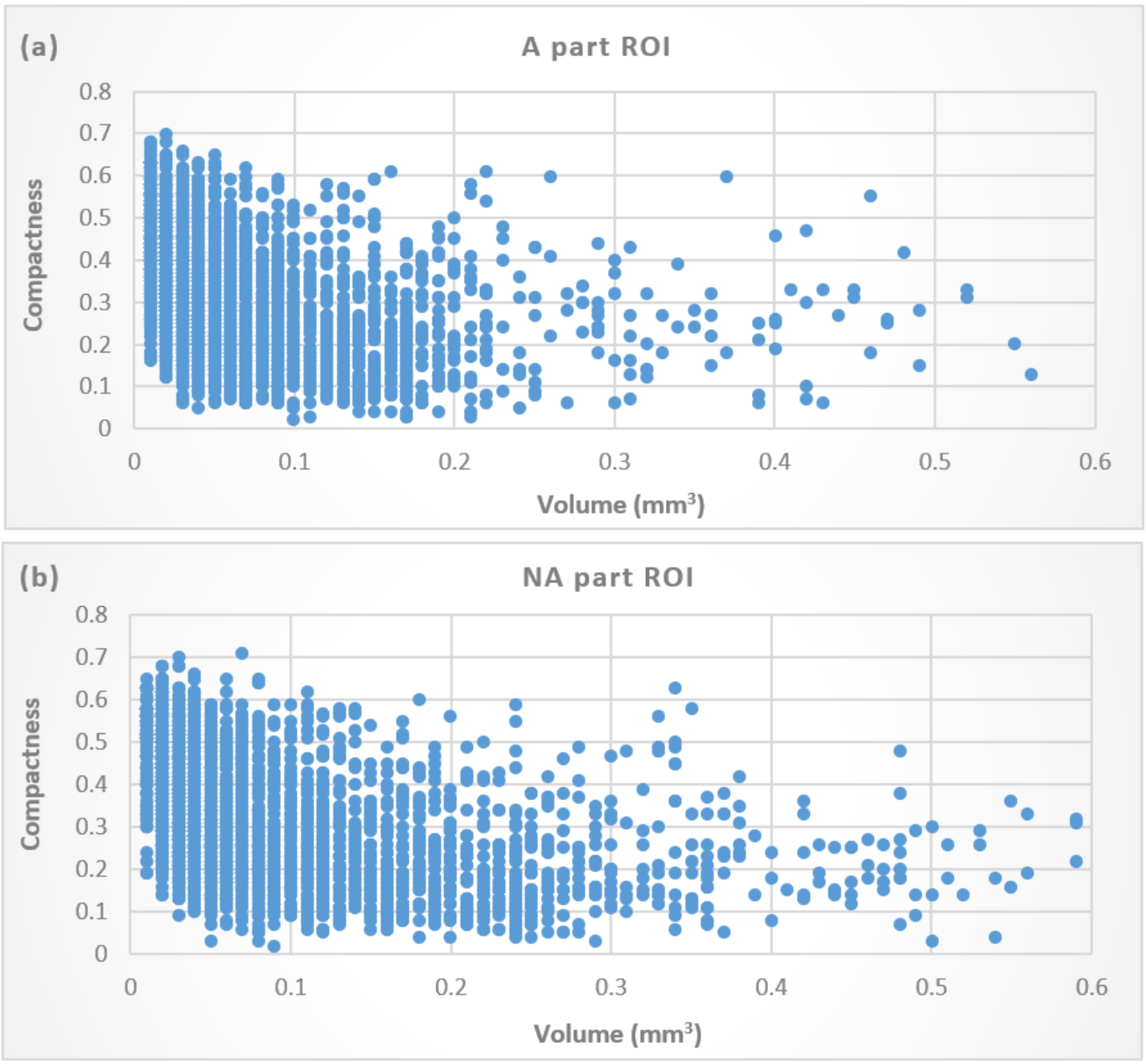

Figure 8.
Distribution of compactness vs volume in the (a) A and (b) NA part ROIs.

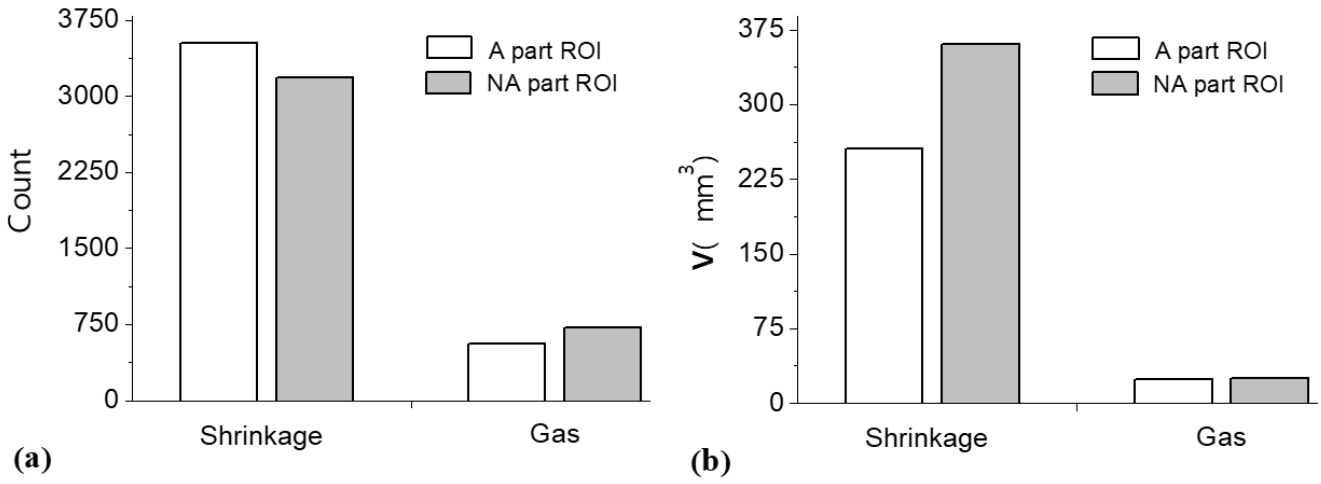

Figure 9.
(a) Count and (b) volume of shrinkage and gas porosity in both ROIs.

Table 2.
Porosity count and volume.

Part	Pore Count	Gas pore count (%)	Shrinkage pore count (%)	Pore volume (mm^3)	Gas pore volume (%)	Shrinkage pore volume (%)
A	4071	8.5	91.5	279.3	13.8	86.2
NA	3881	6.4	93.6	385.1	18.8	81.4

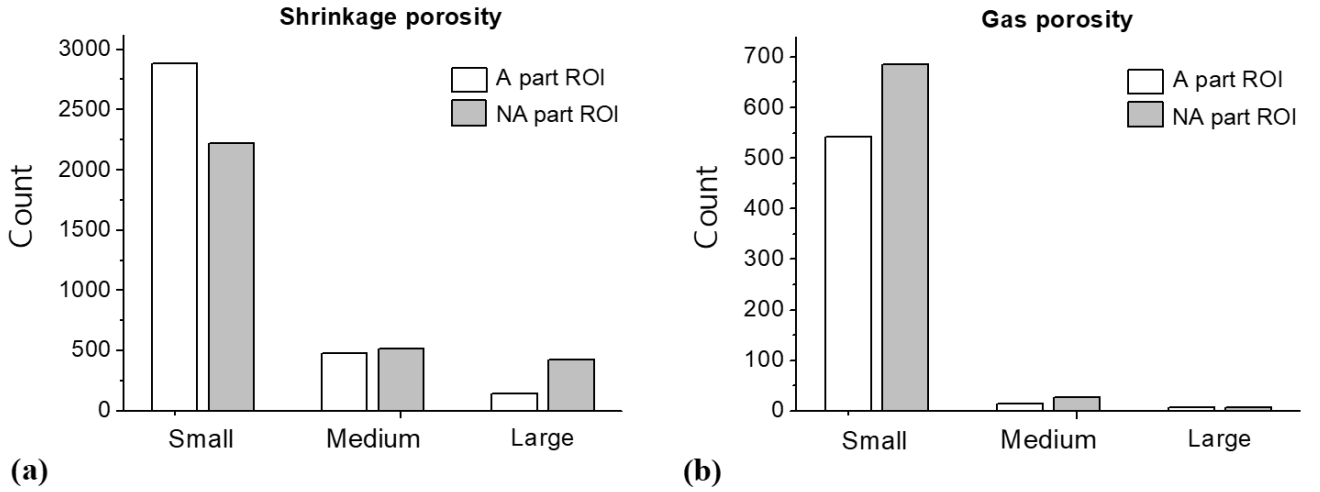

Figure 10.
(a) Shrinkage and (b) gas porosity count in small, medium and large pore subpopulations.

Although the difference in shrinkage pore counts in both ROIs is not high (see Figure 9a), Table 3 shows that the percentage values for the small and large pore subpopulations are significantly different. The ROI corresponding to the A part has a high percentage of small pores and a low percentage of large pores. In contrast, in the NA part ROI, the small pore percentage decreases significantly, and that of large pores increases. The medium-sized pore count shows similar percentage values in both ROIs.

Table 3.
Shrinkage porosity count.

Part	**Small pore count (%)**	**Medium pore count (%)**	**Large pore count (%)**
A	82.3	13.7	4.0
NA	70.3	16.3	13.4

In the case of quasi-spherical pores generated by gas, the count is slightly higher for the NA part ROI (see Figure 9a). Regarding the subpopulations of small, medium, and large pores, the percentage values are similar for both ROIs (Table 4). This would indicate that the excess air during mould filling and the release of gases during the production process were identical for both parts [11]. Furthermore, this anomaly would not be linked to leak-tightness problems. It is worth noting that almost all of the quasi-spherical pores in both ROIs correspond to subpopulations of small pores, which corroborates the porosity shown in the 3D images in Figures 6a and 6c.

3.6. Porosity Volume Analysis

Figure 11 shows the volume corresponding to shrinkage-generated porosity in the small, medium, and large pore subpopulations. In both ROIs, the differences between small and medium pore volumes are not significant. In the case of small pores, the volume occupied by porosity is greater in the A part, which corroborates that small pores do not play a significant role in the leakage problem [11]. However, when the large pore subpopulations are evaluated, the porosity volume is much greater in the NA part ROI. Table 5 shows that the percentage values for the medium pore subpopulations are similar. However, the percentage values for both small and large pores differ significantly in both ROIs. In the A part ROI, more than half of the shrinkage porosity volume corresponds to the small pore subpopulation. In contrast, for the NA part ROI, almost 40% of the porosity volume corresponds to the large pore subpopulation.

Table 4.
Gas porosity count.

Part	**Small pore count (%)**	**Medium pore count (%)**	**Large pore count (%)**
A	96.1	2.5	1.4
NA	95.1	3.7	1.2

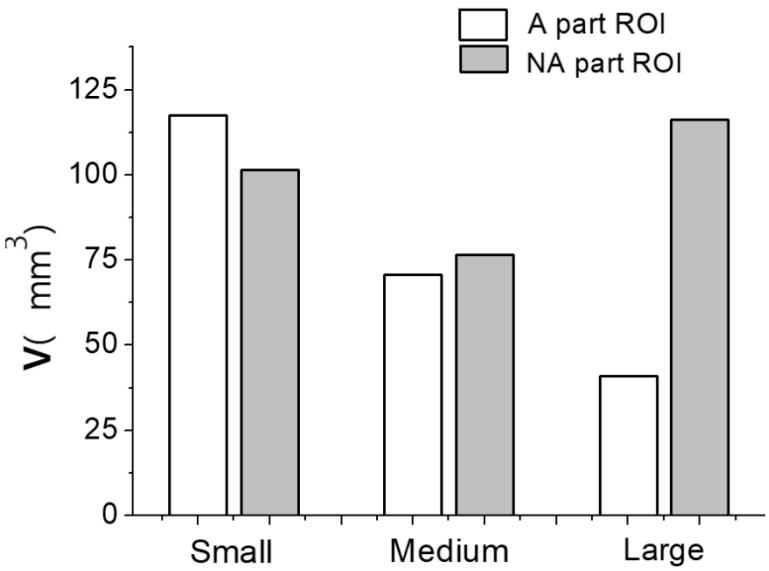

Figure 11.
Shrinkage porosity volume in small, medium and large pore subpopulations.

Table 5.
Shrinkage porosity volume.

Part subpopulation	Small pore volume (%)	Medium pore volume (%)	Large pore volume (%)
A	51.3	30.8	17.9
NA	34.5	26.0	39.5

Table 6 shows the pore volume mean values for the small, medium, and large pore subpopulations. Considering each size category, the mean values are similar for both ROIs. Importantly, the mean values for the small pore subpopulations are very close to the lower limit of the range, which indicates that the pores of these subpopulations are very small. On the other hand, the mean values for the medium pore subpopulations are very close to the midpoint of the range.

Table 6.
Pore volume mean values.

Part	Small pore volume (mm^3)	Medium pore volume (mm^3)	Large pore volume (mm^3)
A	0.041	0.147	0.293
NA	0.046	0.149	0.275

3.7. Gap Parameter Evaluation

Figure 12 shows the distributions of the Gap parameter for the large shrinkage pore subpopulations. It is worth noting that, in both distributions, negative values are a measure of the irregular shape of nearby pores. The distribution of the NA part has a quasi-Gaussian shape, more extended to the right. The count is high for low Gap values, which corroborates the tendency of these pores to cluster. Both distributions are similar at the extremes and the count of the A part distribution is lowest in the range -0.7 to 0.7 mm. Moreover, this distribution is more extended to the right, reaching the high value of 2.8 mm. Furthermore, it is worth noting that both distributions have a similar count for the range 0.7-1.7 mm.

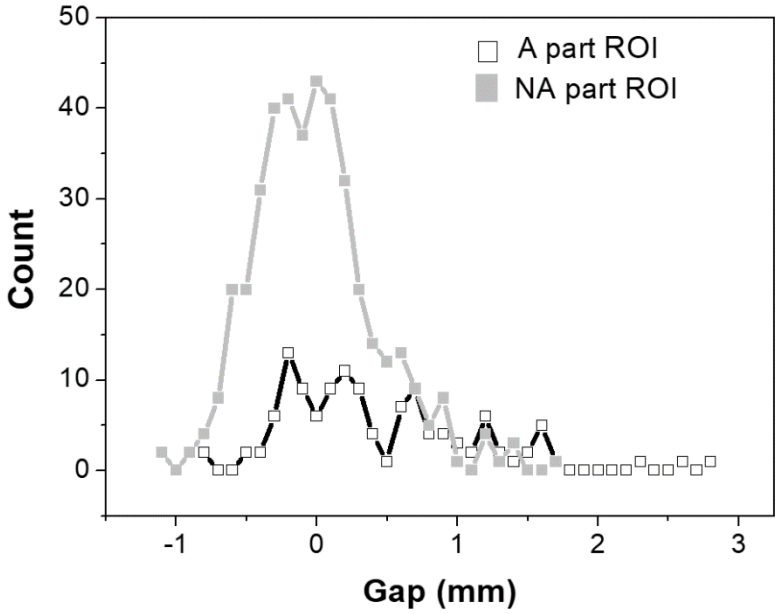

Figure 12.
Gap distributions of the large size shrinkage pore subpopulations.

The high count of small negative values shown in the NA part distribution indicates that the pores are not only irregular but also very close together, which can be corroborated by observing Fig. 8d. This fact reveals thin walls between large pores, so any defect in these walls could open channels between pores [5]. The count values of negative GAP are shown in Table 7. The highest percentage value corresponds to the subpopulation of the NA part, which is almost double that of the A part.

A thorough evaluation of different pore subpopulations, the analysis of the Gap parameter distributions, and the 3D images observed in Figures 6b and 6d indicate that the failures during the procedure carried out to obtain the NA part would be associated with inadequate mould filling and/or cooling. Probably, in this procedure, there were slight modifications in the filling pressure and/or speed in the ROI evaluated, making it impossible to avoid regions of premature solidification, which prevented laminar flow [6]. This fact made it possible that, in that ROI, the volume occupied by large shrinkage pores exceeded the value of 40 mm^3, consequently generating pressurised air leaks during the pneumatic test.

Table 7.
Gap values from large shrinkage pore subpopulations.

Part	Count	Negative Gap pore count	Negative Gap pores (%)
A	124	40	32.3
NA	412	248	60.2

Finally, the methodology proposed in this work, which includes the quantitative study of pore subpopulations generated from the compactness parameter, and the quantitative evaluation of Gap parameter distributions, could be very useful in the stages of research, product development, prototyping and quality control of both cast parts and other porous components obtained from different manufacturing processes.

4. Conclusions

This work proposes a methodology, using X-ray micro-computed tomography and digital image processing, to evaluate subpopulations of shrinkage and gas pores in ROIs of two Al-Si die cast couplings, one accepted and the other rejected for commercialisation. The main conclusions are as follows:

- The boundary compactness value (C = 0.5) between the quasi-spherical and irregular shapes is corroborated by tomographic images of pores from both couplings.
- In the ROI of the A part, solidification was more efficient at the end of the liquid metal feed path (upper zone of the vent cone).
- In both ROIs, the shrinkage pore count is greater than the gas-generated pore count, and the gas porosity volumes are similar.
- In the subpopulations of small, medium, and large pores generated by gas, the percentage values are similar for both ROIs, revealing that the air in excess during mould filling and the gas release during the production process were identical for both parts.

- The volume occupied by large shrinkage pores is high in the ROI of the NA part. Almost 40% of the shrinkage porosity volume in this ROI corresponds to the large pore subpopulation, which would indicate modifications in the mould filling pressure and/or speed that affected solidification.
- Finally, the methodology proposed in this work, which has proven to be very efficient for comprehensively evaluating pore subpopulations in Al-Si castings, could be used to study the quality of other cast alloys and of other porous materials obtained from different manufacturing processes.

References

[1] N. Kumar and S. Panigrahi, "A casting strategy to develop high-performance Al-Si cast alloy," *Manufacturing Letters*, vol. 44, pp. 1731-1738, 2025. https://doi.org/10.1016/j.mfglet.2025.06.192

[2] K. Li *et al.*, "Microstructure evolution of eutectic Si in Al-7Si binary alloy by heat treatment and its effect on enhancing thermal conductivity," *Journal of Materials Research and Technology*, vol. 9, no. 4, pp. 8780-8786, 2020. https://doi.org/10.1016/j.jmrt.2020.06.021

[3] Y. Li, J. Liu, H. Zhou, and W. Huang, "Study on the distribution characteristics of microstructure and mechanical properties within the cylinder head of low-pressure sand cast aluminum alloy," *International Journal of Metalcasting*, vol. 16, no. 3, pp. 1252-1264, 2022. https://doi.org/10.1007/s40962-021-00678-5

[4] R. N. Lumley, N. Deeva, R. Larsen, J. Gembarovic, and J. Freeman, "The role of alloy composition and T7 heat treatment in enhancing thermal conductivity of aluminum high pressure diecastings," *Metallurgical and Materials Transactions A*, vol. 44, no. 2, pp. 1074-1086, 2013. https://doi.org/10.1007/s11661-012-1443-7

[5] M. T. D. Giovanni, J. T. O. d. Menezes, E. Cerri, and E. M. Castrodeza, "Influence of microstructure and porosity on the fracture toughness of Al-Si-Mg alloy," *Journal of Materials Research and Technology*, vol. 9, no. 2, pp. 1286-1295, 2020. https://doi.org/10.1016/j.jmrt.2019.11.055

[6] V. Deev *et al.*, "The influence of the melt cooling rate on shrinkage behaviour during solidification of aluminum alloys," *IOP Conference Series: Materials Science and Engineering*, vol. 537, no. 2, p. 022080, 2019.

[7] L. Elwin and E. Rooy, "Mechanisms of porosity formation in aluminum," *Modern Casting*, vol. 82, pp. 34–36, 1992.

[8] M. Djurdjevic, R. Hasenbusch, and J. Sokolowski, "Assessment of the hydrogen level in 319 aluminum alloy melts using the thermal analysis technique," in *LIGHT METALS-WARRENDALE-PROCEEDINGS-*, 2002, pp. 889-898.

[9] H. Ye, "An overview of the development of Al-Si-alloy based material for engine applications," *Journal of Materials Engineering and Performance*, vol. 12, no. 3, pp. 288-297, 2003. https://doi.org/10.1361/105994903770343132

[10] S. Akhtar, L. Arnberg, M. Di Sabatino, D. Dispinar, and M. Syvertsen, "A comparative study of porosity and pore morphology in a directionally solidified a356 alloy," *International Journal of Metalcasting*, vol. 3, no. 1, pp. 39-52, 2009. https://doi.org/10.1007/BF03355440

[11] A. M. Samuel, E. Samuel, V. Songmene, and F. H. Samuel, "A review on porosity formation in aluminum-based alloys," *Materials*, vol. 16, no. 5, p. 2047, 2023. https://doi.org/10.3390/ma16052047

[12] E. Maire and P. J. Withers, "Quantitative X-ray tomography," *International Materials Reviews*, vol. 59, no. 1, pp. 1-43, 2014. https://doi.org/10.1179/1743280413Y.000000002

[13] R. Hanke, T. Fuchs, M. Salamon, and S. Zabler, "3 - X-ray microtomography for materials characterization," *Materials Characterization Using Nondestructive Evaluation (NDE) Methods*, pp. 45-79, 2016. https://doi.org/10.1016/B978-0-08-100040-3.00003-1

[14] J. Mathew, M. A. Williams, and P. Srirangam, "X-ray computed tomography studies on porosity distribution in vacuum induction cast al-7si alloys," *JOM*, vol. 73, no. 12, pp. 3866-3872, 2021. https://doi.org/10.1007/s11837-021-04944-z

[15] Y. Nikishkov and A. Makeev, "Prior function designs for x-ray computed tomography reconstructions from limited angular views," *Measurement Science and Technology*, vol. 36, no. 5, p. 055405, 2025. https://doi.org/10.1088/1361-6501/adcf43

[16] A. C. Louk, "3D image reconstruction on x-ray micro-computed tomography," *International Conference on Experimental Mechanics 2014*, vol. 9302, pp. 131-137, 2015. https://doi.org/10.1117/12.2081193

[17] F. V. Díaz, M. E. Peralta, and D. O. Fernandino, "Study of sphericity and compactness parameters in spheroidal graphite iron using x-ray micro-computed tomography and image processing," *Journal of Nondestructive Evaluation*, vol. 40, no. 1, p. 11, 2021. https://doi.org/10.1007/s10921-020-00738-6

[18] J. Toledo, F. Diaz, M. Peralta, and D. Fernandino, "High-quality nodule analysis in spheroidal graphite cast iron using X-ray micro-computed tomography," *Fracture and Structural Integrity*, vol. 16, no. 62, pp. 279-288, 2022.

[19] Autoparts, "Air suspension," 2025. https://www.spainautoparts.com/en/blog/air-suspension-comfort-safety-performance#:~:text=What%20is%20Air%20Suspension?,varying%20load%20or%20terrain%20conditions

[20] Geotab, "Air-ride suspension," 2025. https://www.geotab.com/glossary/air-ride-suspension/

[21] K. Stensen and S. Lydersen, "Internal consistency: From alpha to omega?," *Tidsskrift for Den Norske Legeforening*, vol. 142, no. 12, pp. 1–3, 2022. https://doi.org/10.4045/tidsskr.22.0112

[22] C. Muralidhar, M. P. Subramanian, and M. P. V. Ravi Shankar, "Beam hardening effect in computed tomography (CT) – Its relevance and correction in aerospace components," in *Proceedings of 2nd International Conference and Exhibition on Advanced Techniques & Practice of Inspection, NDT & Monitoring, New Delhi*, 2018.

[23] R. A. Ketcham and R. D. Hanna, "Beam hardening correction for X-ray computed tomography of heterogeneous natural materials," *Computers & Geosciences*, vol. 67, pp. 49-61, 2014. https://doi.org/10.1016/j.cageo.2014.03.003

[24] Q. Yang *et al.*, "X-ray attenuation models to account for beam hardening in computed tomography," *Applied Optics*, vol. 59, no. 29, pp. 9126-9136, 2020. https://doi.org/10.1364/AO.402304

[25] H. S. Park, Y. E. Chung, and J. K. Seo, "Computed tomographic beam-hardening artefacts: Mathematical characterization and analysis," *Philosophical Transactions of the Royal Society A: Mathematical, Physical and Engineering Sciences*, vol. 373, no. 2043, p. 20140388, 2015. https://doi.org/10.1098/rsta.2014.0388

[26] Volume graphics, "VGSTUDIO MAX," 2025. https://www.volumegraphics.com/en/products/vgstudio-max.html